Higher-order exceptional lines in a non-Hermitian Jaynes-Cummings triangle

Hao Chen, Xiao Qin, Jian-Jun Dong,* Yu-Yu Zhang,† and Zi-Xiang Hu‡
Department of Physics and Chongqing Key Laboratory for Strongly Coupled Physics, Chongqing University, Chongqing 401331, People's Republic of China

(Received 5 May 2025; accepted 23 September 2025; published 15 October 2025)

Higher-order exceptional points (EPs) in non-Hermitian systems showcase diverse physical phenomena but require more parameter space freedom or symmetries. We report the observation of a third-order exceptional surface and line in a Jaynes-Cummings triangle. A fine-tuning artificial magnetic field enriches the emergence of the third-order exceptional lines (ELs), which require only three tuning parameters when protected by parity-time (PT) symmetry. Third-order ELs maintain robust enhanced sensitivity through a cube-root response mechanism, displaying a greater sensitivity than second-order EPs. We develop a nontrivial fidelity metric based on the biorthogonal associated-state approach that reliably detects EPs while eliminating the unphysical fidelity values in previous approaches. Furthermore, our method captures quench dynamics across EPs, revealing distinct behavior in both PT-symmetric and PT-broken regimes. Our work establishes a platform for studying higher-order geometry in light-matter interactions using circuit QED.

DOI: 10.1103/t49b-s4fs

I. INTRODUCTION

Non-Hermitian (NH) systems such as open or dissipative systems are ubiquitous in nature and have generated great interest in gain-loss coupled cavities [1–3] and photonic platforms [4,5]. Non-Hermiticity leads to various counterintuitive phenomena related to exceptional points (EPs) that cannot exist in Hermitian systems, such as exceptional nodal topologies [6,7], enhanced sensing [8–10], and dynamical quantum phase transition [11–14]. EPs have also been investigated in optical microcavities [15–18] and cold atomic systems [19,20]. So far, most of the work has focused on the basic example of second-order EPs (2EPs) where two eigenstates coalesce. Great experimental efforts have been devoted to exploring 2EPs, particularly in the context of spontaneous PT-symmetry breaking at an EP [5,18,21].

Among the richer phenomena enabled by non-Hermiticity are higher-order EPs [22–24], where three or more eigenvalues coalesce. These singularities are of particular interest due to their pronounced impact on spectral properties, dynamical stability, and response to perturbations. Recent work demonstrated the key advantages of higher-order EPs over conventional second-order EPs, particularly in enhanced sensitivity [24–26]. Prior work primarily focused on isolated higher-order EPs. However, constructing geometries involving higher-order EPs, such as lines composed of higher-order EPs, remains experimentally elusive. Because more degrees of freedom in the Hamiltonian's parameter space or additional symmetries are required. Generally, an nth order EP requires $2n-2$-dimensional real parameter space [27–29]. Recent theoretical and experimental advances demonstrated that generic NH symmetries can reduce the codimension of symmetry-protected nth order EP and ELs [30–32]. EP geometries provide advantages over isolated EPs by relaxing the stringent parameter requirements needed to access exceptional points, thereby enhancing the robustness of EP-related phenomena [33–35].

Recent advances in cavity QED have enabled the synthesis of tunable magnetic fields for light-atom interactions, leading to novel phenomena in a quantum Rabi triangle [36,37] and an anti-Jaynes-Cummings (JC) triangle [38]. Inspired by synthetic magnetic fields, we reveal the emergence of third-order exceptional surfaces and lines naturally emerge in a non-Hermitian JC triangle. The artificial magnetic field is crucial for the observation of the third-order ELs. Quite remarkably, these singularities are unambiguously identified via biorthogonal fidelity and exhibit enhanced sensitivity to perturbations. The quench dynamics across the EPs are successfully characterized by the biorthogonal Loschmidt echo.

II. JC TRIANGLE FOR THIRD-ORDER ELS

Figure 1(a) illustrates a NH system of the JC triangle, composed of three coupled resonators. This setup can be implemented in a circuit-QED architecture using inductively coupled resonators [39–41]. Each superconducting resonator of frequency ω is coupled to a qubit (acting as a two-level system) with a coupling strength g_n. Photons hopping between adjacent cavities are inductively coupled through a mutual capacitance with a hopping strength J_n. PT symmetry is engineered by interconnecting three cavities: two identical cavities with balanced gain and loss, and a neutral central cavity. Here, cavity 1 exhibits amplified gain due to gain medium's lasing, while cavity 3 experiences dissipation-induced loss [1–3]. The JC triangle description holds for weak coupling and hopping strengths ($g_n, J_n \ll \omega$).

*Contact author: dongjianjun@cqu.edu.cn
†Contact author: yuyuzh@cqu.edu.cn
‡Contact author: zxhu@cqu.edu.cn

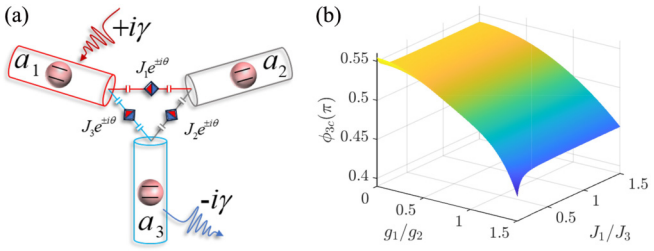

FIG. 1. (a) Schematic of the non-Hermitian JC triangle with an artificial magnetic field $\phi = 3\theta$ in a circuit-QED realization, showing superconducting resonator 1 with gain and resonator 3 with loss. (b) Third-order exceptional surface θ_{3c} as a function of g_1/g_2 and J_1/J_3 with $\Delta/\omega = 20$, $g_2/\omega = 0.03$.

The JC Hamiltonian for each resonator interacting with a two-level system is given by $H_n^{JC} = \omega a_n^\dagger a_n + g_n(a_n^\dagger \sigma_n^- + a_n \sigma_n^+) + \Delta\sigma_n^z/2$, where $a_n^\dagger(a_n)$ denotes the creation (annihilation) operator for resonator n, while σ_n^i are the Pauli matrices representing a two-level system with an transition frequency Δ. H_n^{JC} possesses $U(1)$ symmetry because the excitation number $N = a^\dagger a + \sigma_+\sigma_-$ is conserved. The Hamiltonian consists of the local Hamiltonian for each resonator and the photon hopping term

$$H_{JCT} = \sum_{n=1}^{3} H_n^{JC} + i\gamma a_1^\dagger a_1 - i\gamma a_3^\dagger a_3 - J_n(e^{i\theta} a_n^\dagger a_{n+1} + e^{-i\theta} a_{n+1}^\dagger a_n), \quad (1)$$

where γ denotes the cavity gain-loss constant, and the hopping strength incorporates a phase θ. The artificial vector potential $A(r)$ induces complex hopping amplitudes between cavities n and m, characterized by the phase $\theta = \int_{r_n}^{r_m} A(r)dr$. Artificial magnetic flux can be achieved by periodically modulating the photon hopping strength between adjacent cavities [36]. The magnetic flux across the three cavities is $\phi = 3\theta$, maintaining gauge invariance when traversing the closed loop. When $\theta \neq m\pi$ $m \in \mathbb{Z}$ the time-reversal symmetry of the hopping processes among three cavities is artificially broken, where the time-reversal operator T satisfies $TiT^{-1} = -i$. The system has the PT symmetry, $(PT)H_{JCT}(PT)^{-1} = H_{JCT}$, where the parity operator obeys $P : a_{1(3)} \to a_{3(1)}, a_2 \to a_2$.

We perform the Schrieffer-Wolff transformation using $S_n = \exp[g_n/\Delta(a_n^\dagger\sigma_n^- - a_n\sigma_n^+)]$ to eliminate the off-diagonal coupling term in H_n^{JC}. In the limit $\Delta/\omega \to \infty$, we obtain the transformed Hamiltonian $H_n^{JC} = \omega a_n^\dagger a_n + g_n^2/\Delta a_n^\dagger a_n \sigma_n^z + \Delta\sigma_n^z/2$ by omitting higher-order terms. The low-energy Hamiltonian is given by projecting to the subspace of atom $|\downarrow\rangle_n$ (see Appendix A)

$$H_{JCT}^{\downarrow} = \sum_n -J_n(e^{i\theta} a_n^\dagger a_{n+1} + \text{H.c.}) + \omega_+ a_1^\dagger a_1 + \omega_2 a_2^\dagger a_2 + \omega_- a_3^\dagger a_3, \quad (2)$$

where the renormalized frequency is $\omega_\pm = \omega_1 \pm i\gamma$ with $\omega_n = \omega - g_n^2/\Delta$ by setting $g_1 = g_3$. The Hamiltonian $H_{JCT}^{\downarrow}$ is expressed bilinearly in terms of bosonic operators and can be diagonalized through the Bogoliubov transformation. With denotation $\alpha = \{a_1^\dagger, a_2^\dagger, a_3^\dagger\}$, the Hamiltonian is expressed in matrix form as $H_{JCT}^{\downarrow} = \alpha M \alpha^\dagger$ with a constant, where the matrix M for $J_1 = J_2 \neq J_3$ is given by

$$M = \begin{bmatrix} \omega_+ & -J_1 e^{-i\theta} & -J_3 e^{i\theta} \\ -J_1 e^{i\theta} & \omega_2 & -J_1 e^{-i\theta} \\ -J_3 e^{-i\theta} & -J_1 e^{i\theta} & \omega_- \end{bmatrix}. \quad (3)$$

Eigenenergies can be analytically obtained by diagonalizing M via Cardano's formula (see Appendix B). Given $\chi = (-1 + \sqrt{3}i)/2$ and $\beta_\pm = \sqrt[3]{-q \pm \sqrt{q^2 + p^3}}$, the eigenenergies $E_n = \varepsilon_n + (2\omega_1 + \omega_2)/3$ are given as

$$\varepsilon_1 = \beta_+ + \beta_-, \quad \varepsilon_2 = \chi\beta_+ + \chi^*\beta_-, \quad \varepsilon_3 = \chi^*\beta_+ + \chi\beta_-, \quad (4)$$

where $p = (-2J_1^2 - J_3^2 + \gamma^2)/3 - (\omega_1 - \omega_2)^2/9$, and $q = J_1^2 J_3 \cos(3\theta) - [\omega_2 - \omega_1][(\omega_2 - \omega_1)^2 + 9J_1^2 - 9J_3^2 + 9\gamma^2]/27$.

Notably, NH systems support anomalous singularities called EPs, which play a key role in the real-complex spectral transition protected by PT symmetry. The $q^2 + p^3$ is the key quantity that determines the EPs. PT-symmetry breaking occurs under the condition $q^2 + p^3 = 0$. When $g_1 = g_2$, it yields 2EPs at the critical value

$$\gamma_{2c} = \pm\sqrt{3\sqrt[3]{-\left(J_1^2 J_3 \cos(3\theta)\right)^2} + J_3^2 + 2J_1^2}. \quad (5)$$

Specifically, the 3EPs appear at the special points where $p = q = 0$. It leads to the critical values of the magnetic flux and the gain for the 3ELs, which are obtained analytically as

$$\theta_{3c} = \frac{1}{3}\arccos\left(\frac{(g_2^2 - g_1^2)\left[4(g_2^2 - g_1^2)^2/\Delta^2 + 27J_1^2\right]}{27\Delta J_1^2 J_3}\right), \quad \gamma_{3c}^2 = 2J_1^2 + J_3^2 + \frac{(g_1^2 - g_2^2)^2}{3\Delta^2}. \quad (6)$$

Furthermore, an isolated 3EP arises while $J_1 = J_3 = 0$ and $g_1 = g_2$. Figure 1(b) illustrates the third-order exceptional surface θ_{3c} by adjusting g_1/g_2 and J_1/J_3. When $g_1 = g_2$, the critical magnetic flux simplifies to $\phi_{3c} = 3\theta_{3c} = \pi/2 + n\pi$.

Figure 2 shows the energy spectrum for different θ when $g_1 = g_2$. At the specific magnetic flux $\theta_{3c} = \pi/6$, the eigenenergy E_1 remains real, whereas the other two form complex conjugate pairs above the critical value γ_{3c}, satisfying $\text{Im}[E_2] = -\text{Im}[E_3]$. The line of 3EPs γ_{3c} is located on the curve defined by $q^2 + p^3 = 0$ and $q = 0$, where the real parts of three eigenvalues become equal, $\text{Re}[E_1] = \text{Re}[E_2] = \text{Re}[E_3]$, as depicted in Figs. 2(a) and 2(e). It shows three-state coalescence for any J_1/J_3. For $\gamma > \gamma_{3c}$ and $q^2 + p^3 > 0$, Figs. 2(b) and 2(f) illustrate that two energies form a complex conjugate pair, where $\text{Im}[E_2] = -\text{Im}[E_3]$. Otherwise, for $\theta \neq \theta_{3c}$, the line of 2EPs arises from condition $q^2 + p^3 = 0$ with $q \neq 0$, as illustrated in Figs. 2(c) and 2(d). An isolated 3EP resides at the intersection of two second-order ELs. Along the second-order ELs γ_{2c}, the real components of two eigenvalues merge, whereas E_1 remains distinctly real in Figs. 2(g) and 2(h).

Meanwhile, the 3EP can bifurcate into an additional 2EP by modifying the atom-cavity coupling $g_1 \neq g_2$. When the

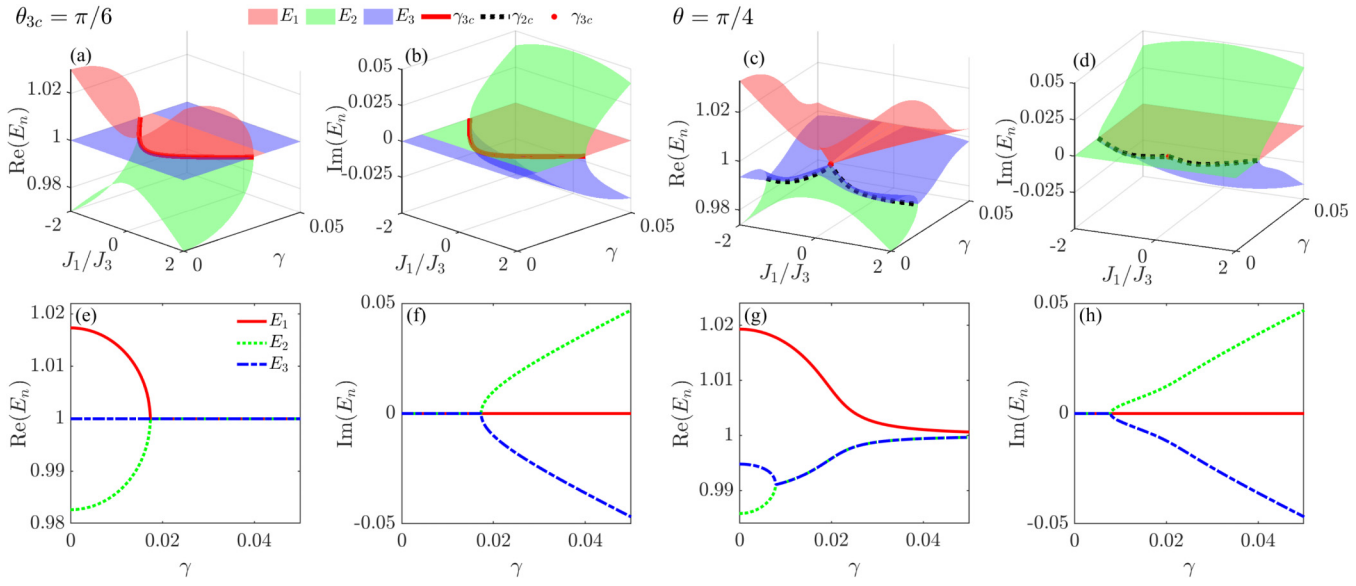

FIG. 2. The colored surfaces represent the eigenenergies for the (a) real Re(E_n) and (b) imaginary Im(E_n) components for $\theta_{3c} = \pi/6$, with respect to gain/loss γ and the hopping ratio J_1/J_3. The red solid line represents the line of 3EPs γ_{3c}. Distinct eigenenergies are shown for $\theta = \pi/4$ in (c) and (d). A red dot marks an isolated 3EP, and a black dashed line represents the second-order ELs γ_{2c}. Re(E_n) and Im(E_n) as a function of γ at the (e) and (f) 3EP and (g) and (h) the 2EP for fixed $J_1/\omega = J_3/\omega = 0.01$. In our calculations, we set $g_1/\omega = g_2/\omega = 0.01$ and $\Delta/\omega = 50$.

coupling strengths in cavities $n = 1, 3$ differ from g_2 in the neutral cavity $n = 2$ in Figs. 3(a) and 3(b), $g_1/g_2 = 0.2$, the eigenstates of the gain and loss cavities, which are separated from that of the cavity 2, coalesce at a 2EP γ_{2c}. Then increasing γ leads to the coalescence of three eigenvalues at a 3EP γ_{3c}. This features an EP formation with tunable cavity-dependent coupling strengths.

III. ENHANCED SENSITIVITY ALONG THE THIRD-ORDER ELS

In NH systems, the eigenenergies splitting exhibits dramatically enhanced response to a perturbation ϵ, scaling as $\epsilon^{1/N}$ where N is the EP order [24,25], producing order-of-magnitude amplification near higher-order EPs. To measure the enhanced sensitivity at the third-order ELs, we introduce a disturbance to the gain cavity ($\epsilon_1 = \epsilon$ and $\epsilon_{2,3} = 0$). The eigenenergies E_n in the equation are given by $E_n^3 - (a+\epsilon)E_n^2 + (b+c\epsilon)E_n + d\epsilon + u = 0$ (see Appendix C). Comparing to the unperturbed eigenenergy E_0 at γ_{3c}, the energy difference $\Delta E_n = E_n - E_0$ constitutes a small correction. We employ a Newton-Puiseux expansion to express this difference as $\Delta E_n = c_1\epsilon^{1/3} + c_2\epsilon^{2/3} + \ldots$ (see Appendix C)

$$\Delta E_n \sim e^{i(2n+1)\pi/3}\eta^{1/3}\epsilon^{1/3} - \frac{v}{3\eta^{1/3}}e^{-i(2n+1)\pi/3}\epsilon^{2/3}, \quad (7)$$

where $\eta = -E_0^2 + (\omega_- + \omega_0)E_0 + J^2 - \omega_0\omega_-$ and $v = \omega_- + \omega_0 - 2E_0$. Then we derive the real part of the energy splitting between E_1 and $E_{2(3)}$, which are analytically expressed as

$$\mathrm{Re}(\Delta E_{12(13)}) \sim \frac{3}{2}\eta^{1/3}\epsilon^{1/3} \pm \frac{\sqrt{3}\gamma_{3c}}{6}\eta^{-1/3}\epsilon^{2/3}. \quad (8)$$

Figure 4(a) shows the real component of the eigenenergies E_n at the 3EP for the perturbing gain cavity for $\theta_{3c} = \pi/6$. The corresponding energy splitting Re(ΔE_{12}) and Re(ΔE_{13}) exhibit a cube-roote scaling in Fig. 4(d), which agree well with the analytical results in Eq. (8). When ϵ appears on the neutral cavity, we also observe the cube-root scaling behavior

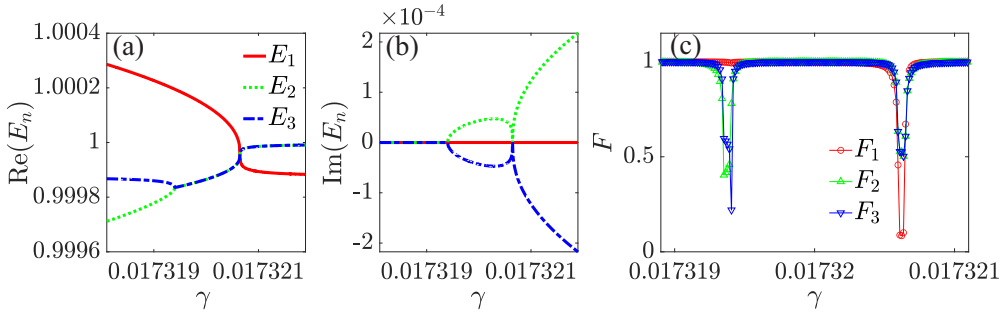

FIG. 3. (a) Real and (b) imaginary parts of E_n as a function of γ for $g_1/\omega = g_3/\omega = 0.01$, $g_2/\omega = 0.05$ and $J_1 = J_3 = 0.01$. A 3EP in Fig. 2 bifurcates into a 2EP at γ_{2c}. (c) Fidelity F_n for three eigenstates between $|\psi_n(\gamma+\epsilon)\rangle$ and $|\psi_n(\gamma)\rangle$ with a small amount $\epsilon = 5 \times 10^{-8}$.

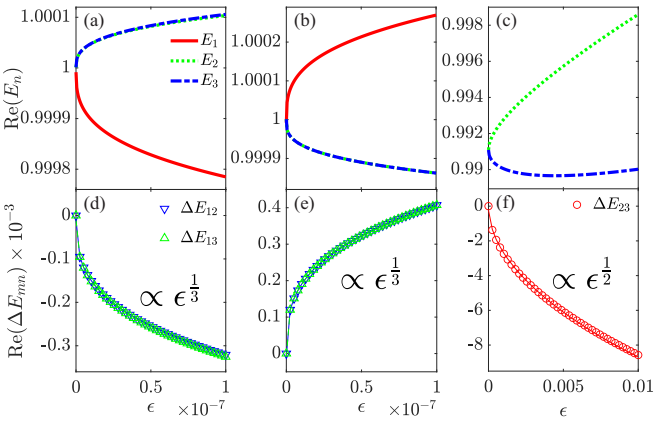

FIG. 4. Real part of E_n and energy splitting $\mathrm{Re}(\Delta E_{12})$, $\mathrm{Re}(\Delta E_{13})$ at the 3EP ($\theta_{3c} = \pi/6$) for the perturbation ϵ on the gain cavity 1 (left column) and the neutral one 2 (middle column), respectively. Right column shows $\mathrm{Re}(E_n)$ and $\mathrm{Re}(\Delta E_{23})$ at the 2EP($\theta = \pi/4$) for the perturbing on the gain cavity. The numerical energy splitting (symbols) fit well with the analytical results (solid lines).

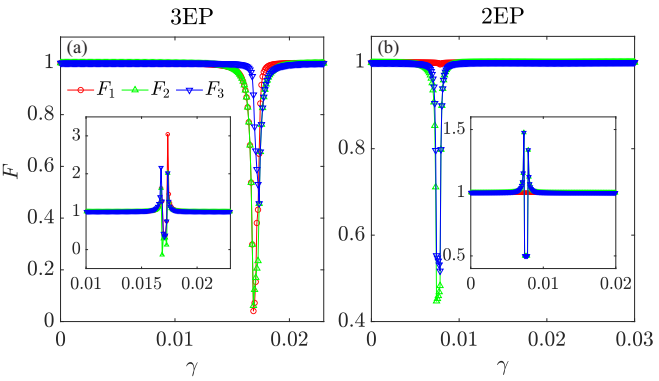

FIG. 5. Fidelity F_n for three eigenstates between $|\psi_n(\gamma+\epsilon)\rangle$ and $|\psi_n(\gamma)\rangle$ for 3EP ($\theta_{3c} = \pi/6$) and 2EP ($\theta = \pi/4$) with a small amount $\epsilon = 5 \times 10^{-4}$. The inserted plots show is fidelity calculated using diagonalization method in Ref. [42].

in Fig. 4(e). At the 2EP, where only eigenvalues E_2 and E_3 coalesce, the energy difference under perturbation is given by $\Delta E_{2(3)} = E_{2(3)} - E_0$. It can be expanded in powers of ϵ as $\Delta E_{2(3)} \sim c_1\epsilon^{1/2} + c_2\epsilon$. The real part of the energy splitting between E_2 and E_3 is derived analytically as

$$\mathrm{Re}(\Delta E_{23}) \sim \mathrm{Re}(-2\sqrt{\alpha})\epsilon^{1/2}, \tag{9}$$

where $\alpha = -\sqrt{9(E_0-\omega_+)^2 - 5(\omega_0+\omega_- - 2E_0)^2}/5 - 3(E_0-\omega_+)/5$. Figure 4(c) shows eigenenergies E_2 and E_3 varing with ϵ at the 2EP for the perturbing gain cavity. The corresponding energy splitting $\mathrm{Re}(\Delta E_{23})$ exhibits the square-root behavior in Fig. 4(f), which is consistent with analytical results in Eq. (9). Consequently, the cube-root scaling of the 3EPs demonstrates significantly enhanced sensitivity compared to the square-root scaling of the 2EPs. Morover, continuous 3ELs maintain robust enhanced sensitivity in the extended parameter space, where most perturbations merely shift the operating point along the 3EL itself, ensuring unprecedented robustness. This intrinsic stability provides decisive advantages over isolated EPs for quantum sensing applications.

IV. ASSOCIATED-STATE BIORTHOGONAL FIDELITY

Fidelity is used as an estimation of the similarity of two quantum states, exhibiting a quick drop at critical points. However, the fidelity loses its conventional meaning in non-Hermitian system, as the standard inner product of quantum mechanics leads to unphysical behavior. For a non-Hermitian Hamiltonian $H \neq H^\dagger$, the eigenvalues equations of H and $H^\dagger$ are given by $H|\psi_n\rangle = E_n|\psi_n\rangle$ and $H^\dagger|\widetilde{\psi}_n\rangle = E_n^*|\widetilde{\psi}_n\rangle$, where $|\psi_n\rangle$ and $\langle\widetilde{\psi}_n|$ are the right and left eigenstates of H that satisfy the biorthonormal relation $\langle\widetilde{\psi}_m|\psi_n\rangle = \delta_{mn}$ and the completeness relation $\sum_n |\widetilde{\psi}_n\rangle\langle\psi_n| = 1$. To generalize the fidelity for non-Hermitian systems, we propose the biorthogonal Fidelity in the framework of the associated-state biorthogonal method

$$F(\gamma) = \frac{\langle\widetilde{\psi}(\gamma)|\psi(\gamma+\epsilon)\rangle\langle\widetilde{\psi}(\gamma+\epsilon)|\psi(\gamma)\rangle}{\langle\widetilde{\psi}(\gamma+\epsilon)|\psi(\gamma+\epsilon)\rangle\langle\widetilde{\psi}(\gamma)|\psi(\gamma)\rangle}, \tag{10}$$

where ϵ is a small quantity and $|\psi(\gamma)\rangle$ is an eigenstate. The perturbative state $|\psi(\gamma+\epsilon)\rangle$ can be expressed as [11]

$$|\psi(\gamma+\epsilon)\rangle = \sum_n a_n|\psi_n(\gamma)\rangle, \tag{11}$$

its associated state $|\widetilde{\psi}(\gamma+\epsilon)\rangle$ and dual state $\langle\widetilde{\psi}(\gamma+\epsilon)|$ can be written as

$$|\widetilde{\psi}(\gamma+\epsilon)\rangle = \sum_n a_n|\widetilde{\psi}_n(\gamma)\rangle,$$
$$\langle\widetilde{\psi}(\gamma+\epsilon)| = \sum_n a_n^*\langle\widetilde{\psi}_n(\gamma)|, \tag{12}$$

with $a_n = \langle\widetilde{\psi}_n(\gamma)|\psi(\gamma+\epsilon)\rangle$.

Figure 5 shows that all three eigenstates undergo a significant decline within the fidelity value [0, 1] at the 3EP γ_{3c}, while two exhibit a marked decrease at γ_{2c}. The 3EP indicates that each of the three state-dependent curves experiences a pronounced drop near γ_{3c}, marking significant changes at the critical point. In contrast, the 2EP exhibits a subtler behavior. Here two curves exhibit significant drop near γ_{2c}, whereas the other curve remains nearly at 1, indicating that this component of the system is largely unaffected by the criticality at these specific EPs. Thus, the fidelity can distinctly detect the emergence of the 3EP and 2EP, as shown in Fig. 3(c). In addition, the conjugate state $\langle\widetilde{\psi}(\gamma+\epsilon)|$ can be obtained by diagonalizing $H^\dagger(\gamma+\epsilon)$. The inserted plots demonstrate that the second method for calculating fidelity can yield unexpected outcomes [42], notably producing real numbers exceeding 1. This contradicts the standard interpretation of fidelity values as probabilities restricted to the interval [0, 1].

Moreover, there are also other different definitions of the fidelity in non-Hermitian quantum systems [42–47], as shown in Table I. Except for the third row of definitions, all other definitions take into account the biorthogonality of non-Hermitian systems. These definitions produce real numbers beyond the interval [0, 1], and even complex numbers,

TABLE I. Comparison of various definitions of the fidelity in non-Hermitian quantum systems.

Formula	Range	Reference
$F=\frac{\langle\widetilde{\psi}(\gamma)\vert\psi(\gamma+\epsilon)\rangle\langle\widetilde{\psi}(\gamma+\epsilon)\vert\psi(\gamma)\rangle}{\langle\psi(\gamma+\epsilon)\vert\psi(\gamma+\epsilon)\rangle\langle\psi(\gamma)\vert\psi(\gamma)\rangle}$	[0, 1]	This work
$F=\langle\widetilde{\psi}(\gamma)\vert\psi(\gamma+\epsilon)\rangle\langle\widetilde{\psi}(\gamma+\epsilon)\vert\psi(\gamma)\rangle$	$\mathbb{C}$	[42]
$F=\langle\psi(\gamma)\vert\psi(\gamma+\epsilon)\rangle\langle\psi(\gamma+\epsilon)\vert\psi(\gamma)\rangle$	[0, 1]	[43]
$F=\frac{1}{2}\vert\langle\widetilde{\psi}(\gamma)\vert\psi(\gamma+\epsilon)\rangle+\langle\psi(\gamma)\vert\widetilde{\psi}(\gamma+\epsilon)\rangle\vert$	$\mathbb{R}^+$	[44]
$F=\sqrt{\vert\langle\widetilde{\psi}(\gamma)\vert\psi(\gamma+\epsilon)\rangle\langle\widetilde{\psi}(\gamma+\epsilon)\vert\psi(\gamma)\rangle\vert}$	$\mathbb{R}^+$	[45]
$F=\sqrt{\langle\widetilde{\psi}(\gamma)\vert\psi(\gamma+\epsilon)\rangle\langle\widetilde{\psi}(\gamma+\epsilon)\vert\psi(\gamma)\rangle}$	$\mathbb{C}$	[46]

further complicating the interpretation of the fidelity in this context. Compared with other definitions, our biorthogonal fidelity based on the associate state is a more robust theoretical framework for the definition of fidelity in the NH systems within the range [0, 1], giving a more reasonable value and meeting the probability interpretation of fidelity satisfactorily.

V. ASSOCIATED-STATE BIORTHOGONAL LOSCHMIDT ECHO

Similarly to the fidelity, the Loschmidt echo is used to quantify the sensitivity of quantum evolution to perturbations. For a quantum quench dynamics, the Hamiltonian changes abruptly from H^i at $t=0^-$ to H^f at $t=0^+$, the eigenstate $|\psi_n^i\rangle$ of H^i will be evolved under the postquench Hamiltonian $|\psi_n^i(t)\rangle=e^{-iH^f t}|\psi_n^i\rangle$. It can be expanded as $|\psi_n^i(t)\rangle=\sum_m d_{nm}|\psi_m^i\rangle$, and the coefficient is given by

$$d_{nm}=\langle\widetilde{\psi}_m^i|\psi_n^i(t)\rangle, \tag{13}$$

which can be explicitly expressed as $d_{nm}=\sum_l e^{-iE_l^f t}\langle\widetilde{\psi}_m^i|\psi_l^f\rangle\langle\widetilde{\psi}_l^f|\psi_n^i\rangle$ in terms of eigenvalue E_l^f and eigenstate $|\psi_l^f\rangle$ of H^f. However, the direct generalization $|\widetilde{\psi}(t)\rangle=e^{-iH^{f\dagger}t}|\widetilde{\psi}(0)\rangle$ leads to unreasonable complex probabilities in the PT breaking regime [11,14]. We define the time-evolved associated state as [11]

$$|\widetilde{\psi}_n^i(t)\rangle=\sum_m d_{nm}|\widetilde{\psi}_m^i\rangle, \tag{14}$$

and its dual state $\langle\widetilde{\psi}_n^i(t)|=\sum_m d_{nm}^*\langle\widetilde{\psi}_m^i|$.

The overlap between the initial state $|\psi(0)\rangle=|\psi_n^i\rangle$ and the time-evolved state $|\psi_n^i(t)\rangle$ can be characterized by the biorthogonal Loschmidt echo

$$\begin{aligned}\mathcal{L}_n(t)&=\frac{\langle\widetilde{\psi}(0)|\psi_n^i(t)\rangle\langle\widetilde{\psi}_n^i(t)|\psi(0)\rangle}{\langle\widetilde{\psi}_n^i(t)|\psi_n^i(t)\rangle\langle\widetilde{\psi}(0)|\psi(0)\rangle}\\&=\frac{|\langle\widetilde{\psi}_n^i|\psi_n^i(t)\rangle|^2}{\langle\widetilde{\psi}_n^i(t)|\psi_n^i(t)\rangle},\end{aligned} \tag{15}$$

where the denominator can be calculated as $\langle\widetilde{\psi}_n^i(t)|\psi_n^i(t)\rangle=\sum_{jm}d_{nm}d_{nj}^*\langle\widetilde{\psi}_j^i|\psi_m^i\rangle=\sum_m d_{nm}d_{nm}^*$. We obtain $\mathcal{L}_n(t)\in[0,1]$ for three initial eigenstate $|\psi_n^i\rangle$ as in the Hermitian case.

Figures 6(a) and 6(b) show the biorthogonal Loschmidt echo for the quenches with both the initial Hamiltonian H^i and the postquench Hamiltonian H^f in the PT-symmetric regime, while in Figs. 6(c) and 6(d) correspond to the case where both are in the PT-broken regime. For H^i in the PT symmetric regime, two identical curves $\mathcal{L}_1(t)$ and $\mathcal{L}_2(t)$ arise in the system with a 3EP ($\theta_{3c}=\pi/6$), while distinct curves $\mathcal{L}_n(t)$ are observed for the 2EP case ($\theta=\pi/4$) in Figs. 6(a) and 6(b). The identical curves likely stem from the symmetry present in the eigenenergy spectrum. When H^f resides in the PT symmetric regime, $\mathcal{L}_n(t)$ exhibits periodic oscillations, while it tends to a steady state for H^f in the PT-broken regime due to the complex eigenenergy E_n^f, as shown in Figs. 6(c) and 6(d). The significance of the postquench Hamiltonian H^f arises from the inclusion of the term $e^{-iE_n^f t}$ in the coefficient d_{nm}.

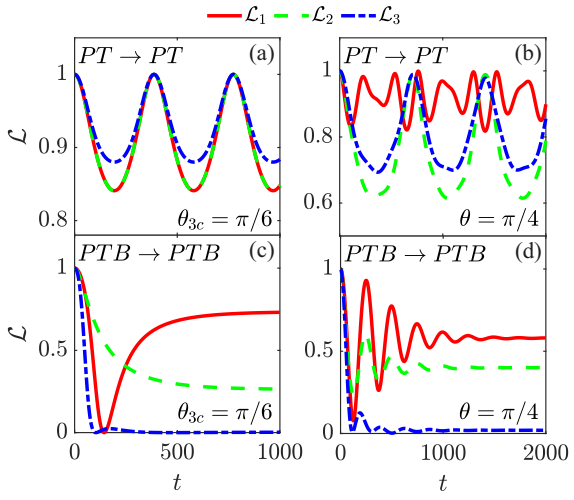

FIG. 6. Loschmidt echo of quenching processes by changing γ (a) from $\gamma_i=0.001$ to $\gamma_f=0.006$ ($\theta_{3c}=\pi/6$); (b) from $\gamma_i=0.006$ to $\gamma_f=0.001$ ($\theta=\pi/4$) in the PT-symmetric regime; and (c) from $\gamma_i=0.05$ to $\gamma_f=0.018$ ($\theta_{3c}=\pi/6$); (d) from $\gamma_i=0.05$ to $\gamma_f=0.01$ ($\theta=\pi/4$) in the PT-broken regime. The initial states are prepared in three eigenstates of H^i. Here, $g_1/\omega=g_2/\omega=0.01$, $J_1=J_3=0.01$, and $\Delta/\omega=50$.

Figure 7 shows distinct quench dynamics by changing γ across both the 3EP and 2EP. When the Hamiltonian is quenched from the PT-symmetric to the PT-broken regime across the 3EP, the Loschmidt echo tends toward two steady-state values in Fig. 7(a). This contrasts with the dynamics across the 2EP in Fig. 7(b), which exhibits three steady states as a consequence of three distinct eigenstates and eigenvalues. Conversely, periodic oscillations emerge in the $\mathcal{L}_n(t)$ for the quenches from the PT-broken to the PT-symmetric regime across both the 3EP and 2EP in Figs. 7(c) and 7(d), resulting from the real eigenenergies E_n^f of the postquench Hamiltonian H^f in the PT-symmetric regime.

VI. CONCLUSION

We presented an unprecedented example of a non-Hermitian light-atom interaction system exhibiting high-order EP geometry within a one-dimensional JC triangle. The JC triangle, with its artificial magnetic field and the PT symmetry, reveals a complexity of EP-related phenomena. Unique singularities at lines of 3EPs exhibit greater sensitivity over 2ELs.

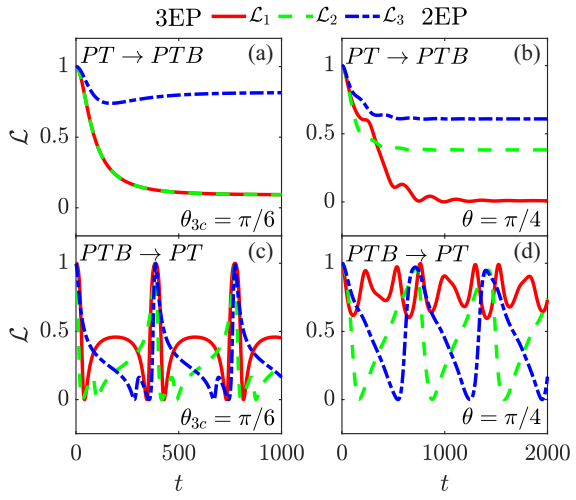

FIG. 7. Loschmidt echo of quenching processes across the 3EP ($\theta_{3c} = \pi/6$) (a) from $\gamma_i = 0.006$ to $\gamma_f = 0.018$ and (c) its reversal dynamics, and cross the 2EP ($\theta = \pi/4$) (b) from $\gamma_i = 0.001$ to $\gamma_f = 0.01$ and (d) its reversal process. We choose three eigenstates of H^i as initial states.

The associated-state biorthogonal fidelity and Loschmidt echo are proposed to characterize the singularities and distinct dynamics across the 3EP even in the PT-broken regime. The realization of high-order exceptional lines with improved sensitivity suggests promising future applications in quantum technologies and ultrasensitive sensors related to light-matter interactions.

ACKNOWLEDGMENTS

This work was supported by National Natural Science Foundation of China under Grants No. 12475013, No. 12075040, No. 12474140, No. 11974064, No. 12204075, No. 12147102, and No. 12347101; Chongqing Natural Science Foundation Grants No. cstc2020jcyj-msxmX0890 and No. CSTB2023NSCQ-MSX0953; and the Fundamental Research Funds for the Central Universities Grant No. 2024CDJXY022.

DATA AVAILABILITY

The data that support the findings of this article are not publicly available. The data are available from the authors upon reasonable request.

APPENDIX A: SCHRIEFFER-WOLFF TRANSFORMATION FOR THE EFFECTIVE HAMILTONIAN OF THE JAYNES-CUMMINGS TRIANGLE

In this appendix, we derive the effective Hamiltonian of the JC triangle given in Eq. (2) of the main text. The Hamiltonian of the JC triangle is $H_{JCT} = \sum_{n=1}^{3} H_n^{JC} + H_{n,n+1}$, where $H_{n,n+1} = -J_n(e^{i\theta} a_n^\dagger a_{n+1} + \text{H.c.})$ describes the photon hopping between the adjacent resonators. The JC Hamiltonian for each resonator is given by $H_n^{JC} = H_n^0 + g_n V$, where

$$H_n^0 = \omega_n' a_n^\dagger a_n + \frac{\Delta}{2}\sigma_n^z, \quad V = a_n^\dagger \sigma_n^- + a_n \sigma_n^+, \tag{A1}$$

where the frequency for the gain and loss cavity are $\omega_{1(3)}' = \omega \pm i\gamma$, and the frequency for the neutral cavity is $\omega_2' = \omega$. We perform the Schrieffer-Wolff transformation with a unitary transformation $U = e^S$, where $S = \sum_{n=1}^{3} \widetilde{g}_n \sqrt{\omega_n'/\Delta}(a_n^\dagger \sigma_n^- - a_n \sigma_n^+)$ with $\widetilde{g}_n = g_n/\sqrt{\Delta\omega_n'}$. It leads to $[H_n^0, S] = -g_n V$. The transformed JC Hamiltonian $\widetilde{H}_{JC} = e^{-S} H_n^{JC} e^S$ is approximately given by

$$\begin{aligned}\widetilde{H}_n^{JC} &= H_n^{JC} + \big[H_n^{JC}, S\big] + \frac{1}{2!}\big[\big[H_n^{JC}, S\big], S\big] + \ldots \\ &= \omega_n' a_n^\dagger a_n + \frac{\Delta}{2}\sigma_n^z + \frac{g_n^2}{\Delta}\left[a_n^\dagger a_n \sigma_n^z + \frac{1}{2}(\sigma_z + 1)\right],\end{aligned} \tag{A2}$$

where the higher-order terms $O(\widetilde{g}_n^2 \omega_n'^2/\Delta)$ are neglected in the frequency limit $\Delta/\omega_n' \to \infty$. Meanwhile, we derive the transformed Hamiltonian of the photon hopping term

$$\begin{aligned}\widetilde{H}_{n,n+1} &= H_{n,n+1} + [H_{n,n+1}, S] + \frac{1}{2!}[[H_{n,n+1}, S], S] + \ldots \\ &= -J_n(e^{i\theta} a_n^\dagger a_{n+1} + \text{H.c.}) + O\big(\widetilde{g}_n^2 J_n \omega_n'/\Delta\big).\end{aligned} \tag{A3}$$

Then we obtain the transformed Hamiltonian for the JC triangle

$$\begin{aligned}\widetilde{H}_n^{JCT} &= \omega_n' a_n^\dagger a_n + \frac{\Delta}{2}\sigma_n^z + \frac{g_n^2}{\Delta}\left[a_n^\dagger a_n \sigma_n^z + \frac{1}{2}(\sigma_z + 1)\right] \\ &\quad - J_n e^{i\theta}(a_n^\dagger a_{n+1} + \text{H.c.}).\end{aligned} \tag{A4}$$

Since the transformed Hamiltonian is free of coupling terms between spin states $|\uparrow\rangle_n$ and $|\downarrow\rangle_n$. By projecting to the subspace of atom $|\downarrow\rangle_n$, we obtain

$$\begin{aligned}H_{JCT}^{\downarrow} &= \sum_{n=1}^{3} -J_n(e^{i\theta} a_n^\dagger a_{n+1} + \text{H.c.}) + \omega_+ a_1^\dagger a_1 \\ &\quad + \omega_2 a_2^\dagger a_2 + \omega_- a_3^\dagger a_3,\end{aligned} \tag{A5}$$

which is Eq. (2) in the main text. The renormalized frequency is $\omega_\pm = \omega_1 + i\gamma$ with $\omega_n = \omega - g_n^2/\Delta$ for the case $g_1 = g_3$.

APPENDIX B: ANALYTICAL SOLUTION OF THE HAMILTONIAN

In this section, we derive the eigenenergies, the critical values of the second-order and three-order exceptional lines in Eqs. (4)–(6). The Hamiltonian $H_{JCT}^{\downarrow}$ in Eq. (2) of the main text can be written in the matrix form as $H_{JCT}^{\downarrow} = \alpha M \alpha^\dagger + C$, where α represents $\{a_1^\dagger, a_2^\dagger, a_3^\dagger\}$ and C is constant. The matrix M is given by

$$M = \begin{bmatrix} \omega_+ & -J_1 e^{-i\theta} & -J_3 e^{i\theta} \\ -J_1 e^{i\theta} & \omega_2 & -J_1 e^{-i\theta} \\ -J_3 e^{-i\theta} & -J_1 e^{i\theta} & \omega_- \end{bmatrix}, \tag{B1}$$

where the hopping amplitude is assumed as $J_1 = J_2 \neq J_3$. Eigenenergies E_n are obtained by solving the determinant

$$\begin{vmatrix} \omega_+ - E_n & -J_1 e^{-i\theta} & -J_3 e^{i\theta} \\ -J_1 e^{i\theta} & \omega_2 - E_n & -J_1 e^{-i\theta} \\ -J_3 e^{-i\theta} & -J_1 e^{i\theta} & \omega_- - E_n \end{vmatrix} = 0. \tag{B2}$$

It leads to the following equation

$$aE_n^3 + bE_n^2 + cE_n + d = 0, \tag{B3}$$

where the corresponding coefficients are

$$\begin{aligned} &a = -1, b = 2\omega_1 + \omega_2, \\ &c = 2J_1^2 + J_3^2 - \left(2\omega_1\omega_2 + \omega_1^2 + \gamma^2\right), \\ &d = \omega_1^2\omega_2 + \omega_2\gamma^2 - J_3^2\omega_2 - 2J_1^2\omega_1 - 2J_1^2J_3\cos(3\theta). \end{aligned} \tag{B4}$$

By defining $E_n = \varepsilon_n + (2\omega_1 + \omega_2)/3$, Eq. (B3) can be expressed as

$$\varepsilon_n^3 + p\varepsilon_n + q = 0, \tag{B5}$$

where coefficients p and q are renormalized as

$$\begin{aligned} p &= \frac{3ac - b^2}{9a^2} \\ &= \left(-2J_1^2 - J_3^2 + \gamma^2\right)/3 - (\omega_1 - \omega_2)^2/9, \\ q &= \frac{27a^2d - 9abc + 2b^3}{54a^3} \\ &= -[\omega_2 - \omega_1]\left[(\omega_2 - \omega_1)^2 + 9J_1^2 - 9J_3^2 + 9\gamma^2\right]/27 \\ &\quad + J_1^2J_3\cos(3\theta). \end{aligned} \tag{B6}$$

The general solutions of Eq. (B5) are analytically obtained using Cardano's formula

$$\begin{aligned} \varepsilon_1 &= \beta_+ + \beta_-, \\ \varepsilon_2 &= \chi\beta_+ + \chi^*\beta_-, \\ \varepsilon_3 &= \chi^*\beta_+ + \chi\beta_-, \end{aligned} \tag{B7}$$

where $\chi = (-1 + \sqrt{3}\mathrm{i})/2$ and $\beta_\pm = \sqrt[3]{-q \pm \sqrt{q^2 + p^3}}$. ε_n corresponds to the eigenenergies in Eq. (4) of the main text.

We analytically derive the third-order exceptional lines(3ELs) by the constraint conditions $q^2 + p^3 = 0$ and $q = 0$. It leads to the critical magnetic flux θ_{3c} and γ_{3c} values

$$\begin{aligned} \theta_{3c} &= \frac{1}{3}\arccos\left(\frac{\left(g_2^2 - g_1^2\right)\left[4\left(g_2^2 - g_1^2\right)^2/\Delta^2 + 27J_1^2\right]}{27\Delta J_1^2 J_3}\right), \\ \gamma_{3c}^2 &= 2J_1^2 + J_3^2 + \frac{\left(g_1^2 - g_2^2\right)^2}{3\Delta^2}, \end{aligned} \tag{B8}$$

which is Eq. (6) of the main text. For the special case of identical couplings ($g_1 = g_2 = g_3$), the coefficients p and q simplify to

$$\begin{aligned} p &= \left(-J_3^2 - 2J_1^2 + \gamma^2\right)/3, \\ q &= J_1^2J_3\cos(3\theta). \end{aligned} \tag{B9}$$

Then the critical magnetic flux reduces to $\phi_{3c} = 3\theta_{3c} = \pi/2 + n\pi$. The second-order exceptional points (2EPs) arise when $q^2 + p^3 = 0$. It gives the critical value

$$\gamma_{2c} = \pm\sqrt{3\sqrt[3]{-\left[J_1^2J_3\cos(3\theta)\right]^2} + J_3^2 + 2J_1^2}, \tag{B10}$$

which is Eq. (5) of the main text.

Figure 8 shows the critical value γ_{3c}, which can be tuned by the atom-cavity coupling ratio g_1/g_2 and hopping strength ratio J_1/J_2.

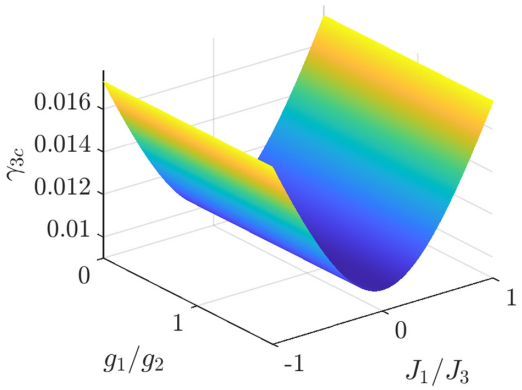

FIG. 8. Third-order exceptional surface γ_{3c} as a function of g_1/g_2 and J_1/J_3 for $\omega = 1$, $\Delta = 20$.

APPENDIX C: EIGENENERGIES FOR THE PERTURBED HAMILTONIAN

To quantify the system's sensitivity to perturbations, we analytically derive Eqs. (7)–(9) of the main text. When the perturbation is induced on the gain cavity ($\epsilon_1 = \epsilon$ and $\epsilon_{2,3} = 0$), the determinant of the Hamiltonian equated to zero gives ($J_1 = J_3 = J$)

$$\begin{vmatrix} \omega_+ - E_n + \epsilon & -Je^{-\mathrm{i}\theta} & -Je^{\mathrm{i}\theta} \\ -Je^{\mathrm{i}\theta} & \omega_0 - E_n & -Je^{-\mathrm{i}\theta} \\ -Je^{-\mathrm{i}\theta} & -Je^{\mathrm{i}\theta} & \omega_- - E_n \end{vmatrix} = 0. \tag{C1}$$

It leads to the equation

$$E_n^3 - (a + \epsilon)E_n^2 + (b + c\epsilon)E_n + d\epsilon + u = 0, \tag{C2}$$

where the parameters are given by $a = \omega_0 + \omega_+ + \omega_-$, $b = -3J^2 + \omega_-\omega_0 + \omega_-\omega_+ + \omega_0\omega_+$, $c = \omega_- + \omega_0$, $d = J^2 - \omega_-\omega_0$, and $u = \omega_-J^2 - \omega_-\omega_0\omega_+ + J^2\omega_0 + J^2\omega_+$.

At the third-order EPs with the critical value γ_{3c} and $\theta_{3c} = \pi/6$, the energy variance $\Delta E_n = E_n - E_0$ is small with respected to the unperturbed eigenenergy E_0. Then Eq. (C2) can be rewritten as

$$\Delta E_n^3 + (r - \epsilon)\Delta E_n^2 + (s + v\epsilon)\Delta E_n + \eta\epsilon + \rho = 0,$$

where the renormalized coefficients are $\rho = -aE_0^2 + bE_0 + E_0^3 + u$, $r = 3E_0 - a$, $s = 3E_0^2 - 2aE_0 + b$, $v = c - 2E_0$, and $\eta = cE_0 + d - E_0^2$. The energy variance ΔE_n can be expressed perturbatively as a Newton-Puiseux series: $\Delta E_n = c_1\epsilon^{1/3} + c_2\epsilon^{2/3}$. It yields

$$\begin{aligned} &c_1s\epsilon^{1/3} + \left(c_1^2r + c_2s\right)\epsilon^{2/3} + \left(c_1^3 + 2c_1c_2r + \eta\right)\epsilon \\ &\quad + \left(3c_1^2c_2 + c_1v + c_2^2r\right)\epsilon^{4/3} + \left(c_2vc_1^2 + 3c_1c_2^2\right)\epsilon^{5/3} \\ &\quad + \left(c_2^3 - 2c_1c_2\right)\epsilon^2 - c_2^2\epsilon^{7/3} = 0. \end{aligned} \tag{C3}$$

By neglecting higher-order terms of ϵ, two sets of equations for the coefficients c_1 and c_2 are obtained by forcing the coefficients of the third and fourth terms to be zero

$$\begin{aligned} c_1^3 + 2c_1c_2r + \eta &= 0, \\ 3c_1^2c_2 + c_1v + c_2^2r &= 0. \end{aligned} \tag{C4}$$

The aforementioned equation yields three distinct solution sets as follows:

$$\left\{c_1\to -\eta^{\frac{1}{3}}, c_2\to -\frac{v}{3c_1}\right\},\quad \left\{c_1\to e^{i\pi/3}\eta^{\frac{1}{3}}, c_2\to -\frac{v}{3c_1}\right\},$$
$$\left\{c_1\to e^{-i\pi/3}\eta^{\frac{1}{3}}, c_2\to -\frac{v}{3c_1}\right\}. \tag{C5}$$

It leads to the energy variance ΔE_n in the form

$$\begin{aligned}\Delta E_1 &\sim -\eta^{1/3}\epsilon^{1/3}+\frac{v}{3\eta^{1/3}}\epsilon^{2/3},\\ \Delta E_2 &\sim e^{-i\pi/3}\eta^{1/3}\epsilon^{1/3}-\frac{v}{3\eta^{1/3}}e^{i\pi/3}\epsilon^{2/3},\\ \Delta E_3 &\sim e^{i\pi/3}\eta^{1/3}\epsilon^{1/3}-\frac{v}{3\eta^{1/3}}e^{-i\pi/3}\epsilon^{2/3},\end{aligned} \tag{C6}$$

which are Eq. (7) in the main text. The energy splitting among three eigenenergies E_n are derived as

$$\begin{aligned}\Delta E_{12} &\sim -\eta^{\frac{1}{3}}\left(\frac{\sqrt{3}}{2}i-\frac{3}{2}\right)\epsilon^{1/3}+\frac{v}{3\eta^{1/3}}\left(\frac{\sqrt{3}}{2}i+\frac{3}{2}\right)\epsilon^{2/3},\\ \Delta E_{13} &\sim \eta^{\frac{1}{3}}\left(\frac{\sqrt{3}}{2}i+\frac{3}{2}\right)\epsilon^{1/3}+\frac{v}{3\eta^{1/3}}\left(-\frac{\sqrt{3}}{2}i+\frac{3}{2}\right)\epsilon^{2/3},\\ \Delta E_{23} &\sim -\eta^{\frac{1}{3}}\sqrt{3}i\epsilon^{1/3}+\frac{v}{3\eta^{1/3}}\sqrt{3}i\epsilon^{2/3}.\end{aligned} \tag{C7}$$

Their real part is given analytically as

$$\begin{aligned}\mathrm{Re}(\Delta E_{12}) &\sim \frac{3}{2}\eta^{1/3}\epsilon^{1/3}+\frac{\sqrt{3}\gamma_{3c}}{6}\eta^{-1/3}\epsilon^{2/3},\\ \mathrm{Re}(\Delta E_{13}) &\sim \frac{3}{2}\eta^{1/3}\epsilon^{1/3}-\frac{\sqrt{3}\gamma_{3c}}{6}\eta^{-1/3}\epsilon^{2/3},\\ \mathrm{Re}(\Delta E_{23}) &\sim \frac{\sqrt{3}\gamma_{3c}}{3}\eta^{-1/3}\epsilon^{2/3},\end{aligned} \tag{C8}$$

which is Eq. (8) in the main text.

For the second-order EPs with the critical value γ_{2c} for $\theta=\pi/4$, Eq. (C2) is modified since the parameter u takes the form $u=\omega_- J^2-\omega_-\omega_0\omega_+-\sqrt{2}J^3(i+1)+J^2\omega_0+J^2\omega_+$, while the other parameters remain the same as those in 3EPs. At the critical value γ_{2c}, the energy variance $\Delta E_{2(3)}-E_0$ follows a power series expansion in the perturbation parameter ϵ: $\Delta E_{2(3)}\sim c_1\epsilon^{1/2}+c_2\epsilon$. Equation (C3) can be reformulated as

$$\begin{aligned}&c_1 s\sqrt{\epsilon}+\left(\eta+c_1^2 r+c_2 s\right)\epsilon+\left(2c_1c_2 r+c_1^3+c_1 v\right)\epsilon^{3/2}\\ &\quad+\left(3c_1^2c_2-c_1^2+c_2^2 r+c_2 v\right)\epsilon^2+\left(3c_1c_2^2-2c_1c_2\right)\epsilon^{5/2}\\ &\quad+\left(c_2^3-c_2^2\right)\epsilon^3=0.\end{aligned} \tag{C9}$$

Similarily, two sets of equations for the coefficients c_1 and c_2 are obtained by forcing the coefficients of the terms $\epsilon^{3/2}$ and ϵ^2 to be zero

$$\begin{aligned}2c_1c_2 r+c_1^3+c_1 v&=0,\\ 3c_1^2c_2-c_1^2+c_2^2 r+c_2 v&=0.\end{aligned} \tag{C10}$$

It yields two sets of solutions for the coefficients c_1 and c_2 as follows:

$$\begin{aligned}&\left\{c_1\to -\sqrt{\alpha}, c_2\to -\frac{\alpha+v}{2r}\right\},\\ &\left\{c_1\to \sqrt{\alpha}, c_2\to -\frac{\alpha+v}{2r}\right\},\end{aligned} \tag{C11}$$

with $\alpha=-\sqrt{9(E_0-\omega_+)^2-5(\omega_0+\omega_--2E_0)^2}/5-3(E_0-\omega_+)/5$. Subsequently, the energy variance $\Delta E_{2(3)}$ is determined

$$\begin{aligned}\Delta E_2 &\sim -\sqrt{\alpha}\epsilon^{1/2}-\frac{\alpha+v}{2r}\epsilon,\\ \Delta E_3 &\sim \sqrt{\alpha}\epsilon^{1/2}-\frac{\alpha+v}{2r}\epsilon.\end{aligned} \tag{C12}$$

The analytical expression for the real part of the energy splitting between E_2 and E_3 is derived as

$$\mathrm{Re}(\Delta E_{23})\sim \mathrm{Re}(-2\sqrt{\alpha})\epsilon^{1/2}. \tag{C13}$$

Inducing perturbations to the other cavities aligns with the above discussed analysis. In the scenario, we also obtain the cubic-root energy splitting between E_1 and $E_{2(3)}$ when a perturbation is applied to the loss cavity ($\epsilon_1=\epsilon_2=0, \epsilon_3=\epsilon$) or the neutral cavity ($\epsilon_1=\epsilon_3=0, \epsilon_2=\epsilon$).

[1] B. Peng, Ş. Kaya Özdemir, F. Lei, F. Monifi, M. Gianfreda, G. L. Long, S. Fan, F. Nori, C. M. Bender, and L. Yang, Parity–time-symmetric whispering-gallery microcavities, Nat. Phys. **10**, 394 (2014).

[2] C. E. Rüter, K. G. Makris, R. El-Ganainy, D. N. Christodoulides, M. Segev, and D. Kip, Observation of parity–time symmetry in optics, Nat. Phys. **6**, 192 (2010).

[3] X.-Y. Lü, H. Jing, J.-Y. Ma, and Y. Wu, $\mathcal{PT}$-symmetry-breaking chaos in optomechanics, Phys. Rev. Lett. **114**, 253601 (2015).

[4] H. Jing, S. K. Özdemir, X.-Y. Lü, J. Zhang, L. Yang, and F. Nori, $\mathcal{PT}$-symmetric phonon laser, Phys. Rev. Lett. **113**, 053604 (2014).

[5] A. Guo, G. J. Salamo, D. Duchesne, R. Morandotti, M. Volatier-Ravat, V. Aimez, G. A. Siviloglou, and D. N. Christodoulides, Observation of $\mathcal{PT}$-symmetry breaking in complex optical potentials, Phys. Rev. Lett. **103**, 093902 (2009).

[6] M. Stålhammar and E. J. Bergholtz, Classification of exceptional nodal topologies protected by $\mathcal{PT}$ symmetry, Phys. Rev. B **104**, L201104 (2021).

[7] K. Ding, G. Ma, Z. Q. Zhang, and C. T. Chan, Experimental demonstration of an anisotropic exceptional point, Phys. Rev. Lett. **121**, 085702 (2018).

[8] Z.-P. Liu, J. Zhang, I. M. C. K. Özdemir, B. Peng, H. Jing, X.-Y. Lü, C.-W. Li, L. Yang, F. Nori, and Y.-X. Liu, Metrology with $\mathcal{PT}$-symmetric cavities: Enhanced sensitivity near the $\mathcal{PT}$-phase transition, Phys. Rev. Lett. **117**, 110802 (2016).

[9] S. Yu, Y. Meng, J.-S. Tang, X.-Y. Xu, Y.-T. Wang, P. Yin, Z.-J. Ke, W. Liu, Z.-P. Li, Y.-Z. Yang, G. Chen, Y.-J. Han, C.-F. Li, and G.-C. Guo, Experimental investigation of quantum $\mathcal{PT}$-enhanced sensor, Phys. Rev. Lett. **125**, 240506 (2020).

[10] J. M. P. Nair, D. Mukhopadhyay, and G. S. Agarwal, Enhanced sensing of weak anharmonicities through coherences in

dissipatively coupled anti-PT symmetric systems, Phys. Rev. Lett. **126**, 180401 (2021).
[11] Y. Jing, J.-J. Dong, Y.-Y. Zhang, and Z.-X. Hu, Biorthogonal dynamical quantum phase transitions in non-Hermitian systems, Phys. Rev. Lett. **132**, 220402 (2024).
[12] K. Wang, X. Qiu, L. Xiao, X. Zhan, Z. Bian, W. Yi, and P. Xue, Simulating dynamic quantum phase transitions in photonic quantum walks, Phys. Rev. Lett. **122**, 020501 (2019).
[13] L. Zhou, Q.-H. Wang, H. Wang, and J. Gong, Dynamical quantum phase transitions in non-Hermitian lattices, Phys. Rev. A **98**, 022129 (2018).
[14] J.-C. Tang, S.-P. Kou, and G. Sun, Dynamical scaling of Loschmidt echo in non-Hermitian systems, Europhys. Lett. **137**, 40001 (2022).
[15] S.-B. Lee, J. Yang, S. Moon, S.-Y. Lee, J.-B. Shim, S. W. Kim, J.-H. Lee, and K. An, Observation of an exceptional point in a chaotic optical microcavity, Phys. Rev. Lett. **103**, 134101 (2009).
[16] B. Peng, S. K. Özdemir, M. Liertzer, and L. Yang, Chiral modes and directional lasing at exceptional points, Proc. Natl. Acad. Sci. USA **113**, 6845 (2016).
[17] Y. Choi, S. Kang, S. Lim, W. Kim, J.-R. Kim, J.-H. Lee, and K. An, Quasieigenstate coalescence in an atom-cavity quantum composite, Phys. Rev. Lett. **104**, 153601 (2010).
[18] L. Jin and F. Xin, Effects of synthetic magnetic flux in a parity-time-symmetric system of three coupled optical resonators, Phys. Rev. A **96**, 043821 (2017).
[19] P. Peng, W. Cao, C. Shen, W. Qu, J. Wen, L. Jiang, and Y. Xiao, Anti-parity–time symmetry with flying atoms, Nat. Phys. **12**, 1139 (2016).
[20] Z. Ren, D. Liu, E. Zhao, C. He, K. K. Pak, J. Li, and G.-B. Jo, Chiral control of quantum states in non-Hermitian spin–orbit-coupled fermions, Nat. Phys. **18**, 385 (2022).
[21] L. Ding, K. Shi, Q. Zhang, D. Shen, X. Zhang, and W. Zhang, Experimental determination of $\mathcal{PT}$-symmetric exceptional points in a single trapped ion, Phys. Rev. Lett. **126**, 083604 (2021).
[22] W. Tang, K. Ding, and G. Ma, Realization and topological properties of third-order exceptional lines embedded in exceptional surfaces, Nat. Commun. **14**, 6660 (2023).
[23] Y. S. S. Patil, J. Höller, P. A. Henry, C. Guria, Y. Zhang, L. Jiang, N. Kralj, N. Read, and J. G. E. Harris, Measuring the knot of non-Hermitian degeneracies and non-commuting braids, Nature (London) **607**, 271 (2022).
[24] H. Hodaei, A. U. Hassan, S. Wittek, H. Garcia-Gracia, R. EI-Ganainy, D. N. Christodoulides, and M. Khajavikhan, Enhanced sensitivity at higher-order exceptional points, Nature (London) **548**, 187 (2017).
[25] W. Chen, Ş. Kaya Özdemir, G. Zhao, J. Wiersig, and L. Yang, Exceptional points enhance sensing in an optical microcavity, Nature (London) **548**, 192 (2017).
[26] X.-G. Wang, G.-H. Guo, and J. Berakdar, Enhanced sensitivity at magnetic high-order exceptional points and topological energy transfer in magnonic planar waveguides, Phys. Rev. Appl. **15**, 034050 (2021).
[27] E. J. Bergholtz, J. C. Budich, and F. K. Kunst, Exceptional topology of non-Hermitian systems, Rev. Mod. Phys. **93**, 015005 (2021).
[28] J. Höller, N. Read, and J. G. E. Harris, Non-Hermitian adiabatic transport in spaces of exceptional points, Phys. Rev. A **102**, 032216 (2020).
[29] P. Delplace, T. Yoshida, and Y. Hatsugai, Symmetry-protected multifold exceptional points and their topological characterization, Phys. Rev. Lett. **127**, 186602 (2021).
[30] R. Okugawa and T. Yokoyama, Topological exceptional surfaces in non-Hermitian systems with parity-time and parity-particle-hole symmetries, Phys. Rev. B **99**, 041202(R) (2019).
[31] J. C. Budich, J. Carlström, F. K. Kunst, and E. J. Bergholtz, Symmetry-protected nodal phases in non-Hermitian systems, Phys. Rev. B **99**, 041406(R) (2019).
[32] Y. Wu, Y. Wang, X. Ye, W. Liu, Z. Niu, C.-K. Duan, Y. Wang, X. Rong, and J. Du, Third-order exceptional line in a nitrogen-vacancy spin system, Nat. Nanotechnol. **19**, 160 (2024).
[33] Q. Zhong, J. Ren, M. Khajavikhan, D. N. Christodoulides, I. M. C. K. Özdemir, and R. El-Ganainy, Sensing with exceptional surfaces in order to combine sensitivity with robustness, Phys. Rev. Lett. **122**, 153902 (2019).
[34] S. Soleymani, Q. Zhong, S. R. M. Mokim, R. El-Ganainy, and Ş. K. Özdemir, Chiral and degenerate perfect absorption on exceptional surfaces, Nat. Commun. **13**, 599 (2022).
[35] K. Ding, C. Fang, and G. Ma, Non-Hermitian topology and exceptional-point geometries, Nat. Rev. Phys. **4**, 745 (2022).
[36] Y.-Y. Zhang, Z.-X. Hu, L. Fu, H.-G. Luo, H. Pu, and X.-F. Zhang, Quantum phases in a quantum Rabi triangle, Phys. Rev. Lett. **127**, 063602 (2021).
[37] D. Fallas Padilla, H. Pu, G.-J. Cheng, and Y.-Y. Zhang, Understanding the quantum Rabi ring using analogies to quantum magnetism, Phys. Rev. Lett. **129**, 183602 (2022).
[38] J.-M. Cheng, Y.-C. Zhang, X.-F. Zhou, and Z.-W. Zhou, Quantum phase transitions in the anti-Jaynes-Cummings triangle model, New J. Phys. **25**, 103048 (2023).
[39] J. Koch, A. A. Houck, K. L. Hur, and S. M. Girvin, Time-reversal-symmetry breaking in circuit-QED-based photon lattices, Phys. Rev. A **82**, 043811 (2010).
[40] A.Nunnenkamp, J. Koch, and S. M. Girvin, Synthetic gauge fields and homodyne transmission in Jaynes–Cummings lattices, New J. Phys. **13**, 095008 (2011).
[41] A. Kamal, J. Clarke, and M. H. Devoret, Noiseless non-reciprocity in a parametric active device, Nat. Phys. **7**, 311 (2011).
[42] Y.-C. Tzeng, C.-Y. Ju, G.-Y. Chen, and W.-M. Huang, Hunting for the non-Hermitian exceptional points with fidelity susceptibility, Phys. Rev. Res. **3**, 013015 (2021).
[43] N. Matsumoto, K. Kawabata, Y. Ashida, S. Furukawa, and M. Ueda, Continuous phase transition without gap closing in non-Hermitian quantum many-body systems, Phys. Rev. Lett. **125**, 260601 (2020).

[44] H. Jiang, C. Yang, and S. Chen, Topological invariants and phase diagrams for one-dimensional two-band non-Hermitian systems without chiral symmetry, Phys. Rev. A **98**, 052116 (2018).

[45] D.-J. Zhang, Q.-H. Wang, and J. Gong, Quantum geometric tensor in $\mathcal{PT}$-symmetric quantum mechanics, Phys. Rev. A **99**, 042104 (2019).

[46] G. Sun, J.-C. Tang, and S.-P. Kou, Biorthogonal quantum criticality in non-Hermitian many-body systems, Front. Phys. **17**, 33502 (2022).

[47] Y.-T. Tu, I. Jang, P.-Y. Chang, and Y.-C. Tzeng, General properties of fidelity in non-Hermitian quantum systems with PT symmetry, Quantum **7**, 960 (2023).